2021-1

A Comparison of Aerodynamic Models for Optimizing the Takeoff and Transition of a Bi-wing Tailsitter

Ryan Anderson
Brigham Young University, rymanderson@gmail.com

Jacob Willis
Brigham Young University, jbwillis1994@gmail.com

Jacob Johnson
Brigham Young University, jacobcjohnson13@gmail.com

Andrew Ning
Brigham Young University, aning@byu.edu

Randal Beard
Brigham Young University, beard@byu.edu

A Comparison of Aerodynamic Models for Optimizing the Takeoff and Transition of a Bi-wing Tailsitter

Ryan Anderson*, Jacob Willis†, Jacob Johnson‡, Andrew Ning§, and Randal Beard¶
Brigham Young University, Provo, Utah, 84602

Electric vertical takeoff and landing (eVTOL) aircraft take advantage of distributed electric propulsion as well as aerodynamic lifting surfaces to take off vertically and perform long-duration flights. Complex aerodynamic interactions and a hard-to-predict transition maneuver from hover to wing-borne flight are one challenge in their development. To address this, we compare three different interaction models of varying fidelity for optimizing the transition trajectory of a biplane tailsitter. The first model accounts for simplified rotor-on-wing interactions using momentum theory, while the other two account for wing-on-wing interactions using a vortex lattice method and rotor-on-wing aerodynamic interactions using blade element momentum theory. One includes the swirl component of velocity and the other neglects swirl. To determine the trajectory, we perform direct collocation on the lowest fidelity model using gradient-based optimization. To compare them, we use the same control inputs obtained in the optimization to integrate trajectories using the higher fidelity models. We find that the higher fidelity models predict power and stall significantly more conservatively than the lowest fidelity model. We conclude that modeling the swirl velocity of the rotor wake and the selected stall model play a significant role in defining the transition trajectory.

Nomenclature

A_d	=	Area swept by a rotor disk
AR	=	Wing aspect ratio
b	=	Wingspan
C_D	=	Wing drag coefficient
C_{D_P}	=	Wing parasitic drag coefficient
C_L	=	Wing overall lift coefficient
$C_{L,\text{stall}}$	=	Wing overall lift coefficient at stall
C_M	=	Wing pitching moment coefficient
C_P	=	Rotor power coefficient
C_Q	=	Rotor torque coefficient
C_T	=	Rotor thrust coefficient
c	=	Wing mean chord
c_l	=	Wing local lift coefficient
$c_{l,\text{stall}}$	=	Wing local lift coefficient at stall
D_P	=	Wing parasitic drag force
d_r	=	Rotor diameter
e_i	=	ith basis vector, having a 1 in the ith position and zeros elsewhere
F	=	Net aerodynamic force vector acting on the vehicle
$f(\mathbf{x}, \mathbf{u})$	=	Vehicle dynamic model
g	=	Gravitational coefficient
I	=	Moment of inertia of the vehicle
J	=	Rotor advance ratio

*Doctoral Candidate, Department of Mechanical Engineering, ryan.anderson@byu.edu, AIAA Member
†Masters Student, Department of Electrical and Computer Engineering, jbwillis272@gmail.com
‡Doctoral Student, Department of Electrical and Computer Engineering, jjohns99@byu.edu.
§Associate Professor, Department of Mechanical Engineering, aning@byu.edu, AIAA Associate Fellow.
¶Professor, Department of Electrical and Computer Engineering, beard@byu.edu, AIAA Associate Fellow.

J_{energy}	=	Trajectory optimization energy objective
M	=	Net aerodynamic moment acting on the vehicle
m	=	Mass of the vehicle
N_t	=	Uniformly spaced time collocation points
n	=	Rotational speed of a rotor in rotations per second
P	=	Power produced by one or more vehicle rotors
p	=	Position vector of the aircraft w.r.t. a fixed inertial frame
R	=	Rotation from the inertial frame to the body frame
S	=	Wing surface area
s	=	Wing separation distance
T	=	Thrust produced by one or more vehicle rotors
t	=	Time
$\mathbf{u}$	=	Control inputs to the VTOL system
V_D	=	Velocity at a rotor disk
V_d	=	Desired airspeed velocity during trim optimization
V_n	=	Freestream velocity component normal to a rotor disk
V_∞	=	Freestream velocity
v	=	Velocity vector of the aircraft w.r.t. a fixed inertial frame
$\mathbf{x}$	=	States of the VTOL system
α	=	Angle of attack
γ	=	Flight path angle
ρ	=	Air density
θ	=	Pitch angle of the aircraft w.r.t. the horizontal
ξ	=	Rotor cant angle
$\dot{*}$	=	Time derivative of variable $*$
$*_f$	=	Final value of variable $*$
$*_{\text{net}}$	=	Net quantity of variable $*$
$*_{\text{lower}}$	=	Quantity of variable $*$ produced by a single rotor on the lower wing
$*_{\text{upper}}$	=	Quantity of variable $*$ produced by a single rotor on the upper wing
$*_0$	=	Initial value of variable $*$

I. Introduction

Electric vertical takeoff and landing (eVTOL) aircraft are being actively developed by many industry and government research groups. These vehicles take advantage of distributed electric propulsion as well as aerodynamic lifting surfaces to take off vertically and perform long duration flights. One challenge in eVTOL design is finding an efficient and stable method to transition from hover to wing-borne flight. Relevant physics of the transition maneuver includes stall in addition to complex, unsteady interactions between rotors, wings, and fuselage. Conventional aerodynamic models that capture such effects such as mesh-based CFD are very computationally expensive, making them ill-suited for optimization. On the other hand, most trajectory analyses use simplified models to make computation less expensive, but sacrifice some of the physical interactions. Because of the complexity of eVTOL aerodynamics, this sacrifice of model fidelity could result in trajectories that are suboptimal or violate the dynamic constraints of the vehicle. We intend to quantify and compare the fidelity of three aerodynamic models as applied to trajectory optimization of the CRC-3, a biplane tailsitter VTOL research vehicle [1, 2] designed at Army Research Laboratories (ARL). This comparison can then be used to inform the appropriate level of model fidelity to use when planning eVTOL trajectories.

Related work on trajectory generation for similar vehicles varies in the degree that aerodynamic effects are considered in the optimization model and in the approach to control. Takeoff trajectory optimization for commercial and military aircaft has been studied for decades. The minimum time-to-climb problem [3] is a typical example, but it assumes the vehicle's aerodynamic surfaces remain close to level. Modern approaches to solving this problem [4] formulate it as a two-point boundary value problem along with a minimum-time objective. This is then solved using a collocation-based optimization method. The example of solving this problem found in [4] considers only commercial or fighter aircraft approaching sonic speeds, and the aerodynamic model used is based on tabulated data. These conditions differ significantly from our problem where we consider the relatively low speed flight of a small UAV which takes off vertically, but we use this optimal control framework in formulating our trajectory optimization.

Nieuwstadt demonstrated modeling, control, and trajectory generation for a three-degree of freedom ducted fan, having similar two dimensional dynamics to the vehicle we present here [5]. Aerodynamics are neglected in the model in order to reduce the computational complexity of the trajectory generation, making the trajectories valid only for low speed maneuvers. To account for aerodynamic interactions, Droandi et al. demonstrated a method for planning the transition of a tilt-wing eVTOL aircraft using a mixed-fidelity, quasi-steady aerodynamic model and smoothing between optimal trim points to find the transition trajectory [6]. A quadrotor with a single wing parallel to the direction of thrust is modeled and the transition from hover to forward flight is optimized in [7]; the aerodynamics use empirically-obtained lift curves and the transition control is designed for a step input command from vertical to horizontal flight. The transitions are found assuming an already hovering state where the vehicle can dip below its initial altitude. Chauhan demonstrated takeoff trajectory optimization of a human-transport-sized tilt-wing eVTOL using this lift curve approach [8] and predicting stall using a model by Tangler and Ostowari [9]. To perform the optimization, the control variables are represented as splines and the dynamics are integrated using Euler integration. Hrishikesh [10] demonstrated a non-optimal transition of a biplane tailsitter in a hardware experiment.

Blown wings experience significant rotor-on-wing and rotor-on-rotor aerodynamic interactions that affect aircraft performance [11, 12]. For example, Witkowski demonstrated that rotor-on-wing interactions can be captured using a quasi-steady vortex lattice method (VLM) [13], and Alvarez demonstrated that rotor-on-rotor interactions may be captured using a vortex particle method [14]. Unsteady wake effects that are not easily captured by quasi-steady models like the VLM can also have a significant effect on aerodynamic performance; for example, Thom et al. showed up to a 40% difference in wing loading due to unsteady interactions [15]. Reddinger demonstrated in simulation that the interaction between rotors and wings of a larger scaled version of the CRC-3 makes possible a transition trajectory that completely avoids stall, and significantly reduces the predicted power requirement. In this study, the rotor wake velocity was obtained using momentum theory and used as the inflow to the wings [16]. McIntosh extended this model to obtain minimum-time trajectories using direct collocation [17].

Similarly to [16] and [17], we investigate the optimality of takeoff and transition trajectories for the CRC-3 aircraft. However, we aim to explore the influence of aerodynamic model fidelity on the performance of the trajectories obtained. We investigate three interaction models, finding energy-optimal trajectories for transition maneuvers. Each model has an increasing level of fidelity. The lowest fidelity model is a quasi-steady model based on pre-computed lift polars and thrust coefficients that neglects rotor-wing and wing-wing aerodynamic interactions. The other models capture some of these interactions using a quasi-steady vortex-lattice method (VLM) for the lifting surfaces and a blade-element momentum (BEM) model for the rotors. One of these includes the swirl component of the rotor wake, and one neglects it. We examine the advantages and disadvantages of each aerodynamic model. The aerodynamic forces and moment obtained from the models are applied to a rigid-body dynamic model for optimization. We approach the takeoff problem from an optimal control standpoint, using trapezoidal direct collocation to integrate the aerodynamics and kinematics through takeoff and transition to level flight. We optimize transition trajectories using the low fidelity model and integrate the obtained control sequence on the mid fidelity models to investigate the impact of using a low fidelity model in optimization. In particular we investigate how stall and power consumption are not properly predicted using a low fidelity optimization model, resulting in suboptimal trajectories.

II. Aerodynamics

Here we model the CRC-3 biplane tailsitter, depicted in Fig. 1. Each rotor is positioned with a 10° inboard cant angle to increase maneuverability during wingborne flight [18]. We consider translation in the forward and upward axis directions only, and we limit rotation to occur only about the pitch axis. We describe each of three aerodynamic models in order of increasing fidelity in the following sections. Because we wish to optimize a trajectory using one model and then simulate trajectories using the other models with the same control inputs, we take care to calibrate the models to behave similarly. More specifically, we tune each model a priori to have the same lift polars in the absence of rotors, and to have the same rotor thrust and power coefficients. Each model differs primarily by its interaction model.

A. Low Fidelity Model

The lowest-fidelity model we employ assumes that coefficients of lift, drag, and pitching moment are predetermined functions only of angle of attack, α. The model also assumes that rotor thrust, torque, and power are functions only of advance ratio, ignoring edge effects. We use momentum theory to predict the average velocity induced by the rotor, which we use to predict rotor-on-wing interactions. We ignore rotor-on-rotor, wing-on-wing, and wing-on-rotor interactions.

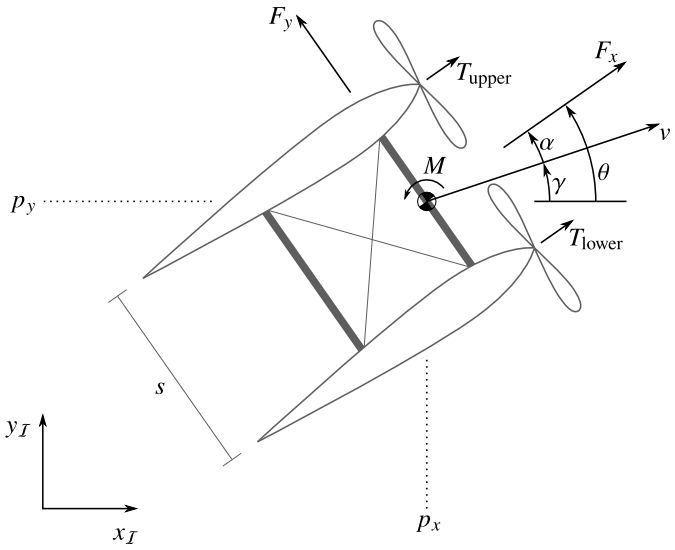

Fig. 1 Notation used for representing the planar bi-wing VTOL.

1. Rotors

For the rotor, we calculate thrust, torque, and power coefficients as a function of advance ratio using the blade-element momentum (BEM) code CCBlade*, to which we fit Akima splines†. We calculate the advance ratio using the freestream component normal to the rotor disk as

$$J = \frac{V_n}{nd_r} \tag{1}$$

with n the rotations per second, d_r the rotor diameter, and $V_n = V_\infty \cos(\alpha)\cos(\xi)$, where α and ξ are the angle of attack and 10° cant angle, respectively, and V_∞ is the freestream velocity at the rotor disk. We use the advance ratio to reference the thrust, moment, and power coefficient (C_T, C_Q, and C_P, respectively) curve fits (see Fig. 2) and obtain the dimensional thrust T and power P required for a single rotor.

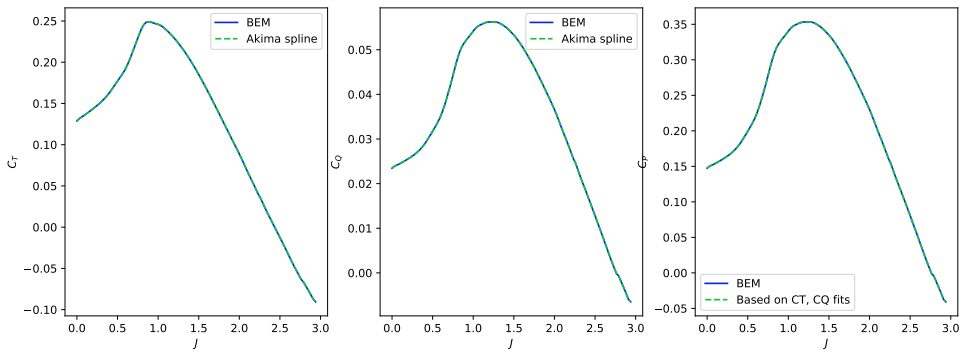

Fig. 2 Akima spline fit of thrust and torque coefficient curves with which power coefficients are computed.

Since we model two rotors on each wing, the net thrust and net power are then evaluated by summing:

$$T_{\text{net}} = 2T_{\text{upper}} + 2T_{\text{lower}} \tag{2}$$

*https://github.com/byuflowlab/CCBlade.jl
†https://github.com/byuflowlab/FLOWMath.jl

$$P_{\text{net}} = 2P_{\text{upper}} + 2P_{\text{lower}} \tag{3}$$

where $*_{\text{upper}}$ and $*_{\text{lower}}$ represent a single rotor on the upper and lower wings, respectively.

According to momentum theory, the velocity at the rotor disk evaluates as

$$V_D = \frac{V_n}{2} + \sqrt{\frac{\rho A_d V_n^2 + 2T}{4\rho A_d}} \tag{4}$$

where A_d is the area swept by the rotor disk, ρ is the air density, and T is the thrust obtained using the quadratic fit mentioned previously. Consequent to the symmetry granted by our 2-D dynamics, we constrain the RPM of both rotors on the same wing to be equal, and use RPM as the control input as described in Sec. III.

2. Wings

We obtain lift, drag, and moment polars for the aircraft using a vortex lattice method (VLM) code [‡] (shown in Fig. 3). Note that we have added parasitic drag to the induced drag computed by the VLM, as described in Sec. II.B.3.

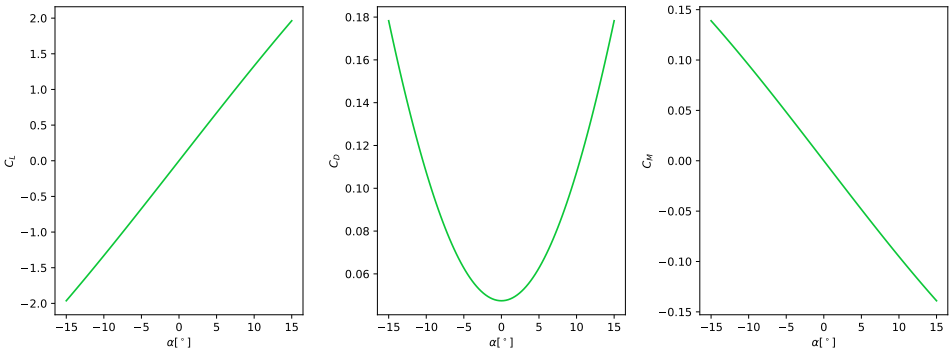

Fig. 3 Lift, drag, and moment polars obtained using the VLM.

Next, we consider wing-rotor interactions. According to momentum theory, the fully-developed wake velocity is twice that at the rotor disk, implying that the velocity of the wake when it interacts with the wing should be somewhere between one and two times its value at the rotor disk. Velduis showed that the swirl velocity remains unchanged for a blown wing, but that the axial component indeed increases as predicted by momentum theory [11]. Studies suggest that a rotor wake develops fully after 1 or more rotor diameters [19, 20]. However, because the rotors are less than a rotor diameter from the wing (actually about 20% of a diameter), we do not expect the wake to develop fully before interacting with the wing. Therefore, we assume that wake velocity is still equal to its value at the rotor disk when it interacts with the wing, and do not apply any correction factor. Because increasing the wake velocity will only serve to decrease the likelihood of stall, we expect this to be a conservative assumption. We also acknowledge that this low fidelity model completely neglects the swirl component of the wake velocity.

Then, because the rotors cover a large percentage of the span, we make V_D the inflow used to compute lift, drag, and moments, assuming the edgewise component of the freestream is unchanged by the rotor, and neglecting any spanwise component of velocity produced by the 10° rotor cant angle. We avoid stall by constraining the wing's lift coefficient to be less than the stall angle of attack, $C_L < C_{L,\text{stall}}$. We obtain $C_{L,\text{stall}}$ by noting the angle of attack at which any wing section's lift coefficient exceeds its stall lift coefficient, $c_l > c_{l,\text{stall}}$

This model provides some prediction of interactions of rotors on wings by applying the average axial wake velocity uniformly across the wing. However, it does not consider the uneven velocity distribution of the rotor wake, nor does it consider rotor upwash and downwash on the wing. It also ignores minor interactions of rotors on rotors and wings on rotors.

[‡] `https://github.com/byuflowlab/VLM.jl`

These assumptions result in the aerodynamic force $F(\mathbf{x}, \mathbf{u})$ and moment $M(\mathbf{x}, \mathbf{u})$:

$$F(\mathbf{x}, \mathbf{u}) = \begin{bmatrix} F_x \\ F_y \end{bmatrix} = \frac{1}{2}\rho \left(V_{\infty_{\text{lower}}}^2 + V_{\infty_{\text{upper}}}^2 \right) S \begin{bmatrix} C_D(\alpha) \\ C_L(\alpha) \end{bmatrix} + \begin{bmatrix} T_{\text{net}} \\ 0 \end{bmatrix} \tag{5}$$

$$M(\mathbf{x}, \mathbf{u}) = \frac{1}{4}\rho \left(V_{\infty_{\text{lower}}} + V_{\infty_{\text{upper}}} \right) ScC_M(\alpha) + \left(2T_{\text{lower}} - 2T_{\text{upper}} \right) s, \tag{6}$$

where $\mathbf{x}$ and $\mathbf{u}$ are the aircraft state and control input vectors (further defined in Section III), C_D, C_L, and C_M are respectively the drag, lift, and pitching moment coefficients, and where $S = \frac{b^2}{\text{AR}}$ is the wing area, $c = \frac{b}{\text{AR}}$ is the mean chord of the wing, s is the spacing between wings, b is the wingspan, and AR is the wing aspect ratio. The freestream velocity for the upper and lower wings will not be the same due to differences between rotor wakes, so we compute them separately.

B. Mid Fidelity

The other two aerodynamic models represent lifting surfaces using a VLM and rotors using a BEM model such that we capture quasi-steady wing-on-wing and rotor-on-wing aerodynamic interactions. In one model, we use CCBlade to predict the wake axial and swirl induced velocities, which we add to the freestream and pass to the VLM solver to obtain lift and drag. For comparison, we ignore the swirl component of velocity in the other mid fidelity model.

1. BEM Rotor Model

CCBlade uses a numerical scheme with guaranteed convergence using a 1-D root-finding algorithm as demonstrated by Ning [21]. We also note that CCBlade applies 3-D correction factors demonstrated by Du for lift [22] and by Eggers for drag [23], as well as a 360° stall extrapolation demonstrated by Viterna [24]. For airfoil lift and drag coefficients, we use tabulated airfoil data obtained at ARL using digital scans of the rotor and the flow solver HAMSTR[25]. In Fig. 4, we show the axial and swirl components, respectively, of the rotor wake over upper and lower wings as a function of advance ratio, normalized by the average velocity at the rotor disk V_D as described in Sec. II.A.1.

The wake becomes less significant at higher advance ratios.

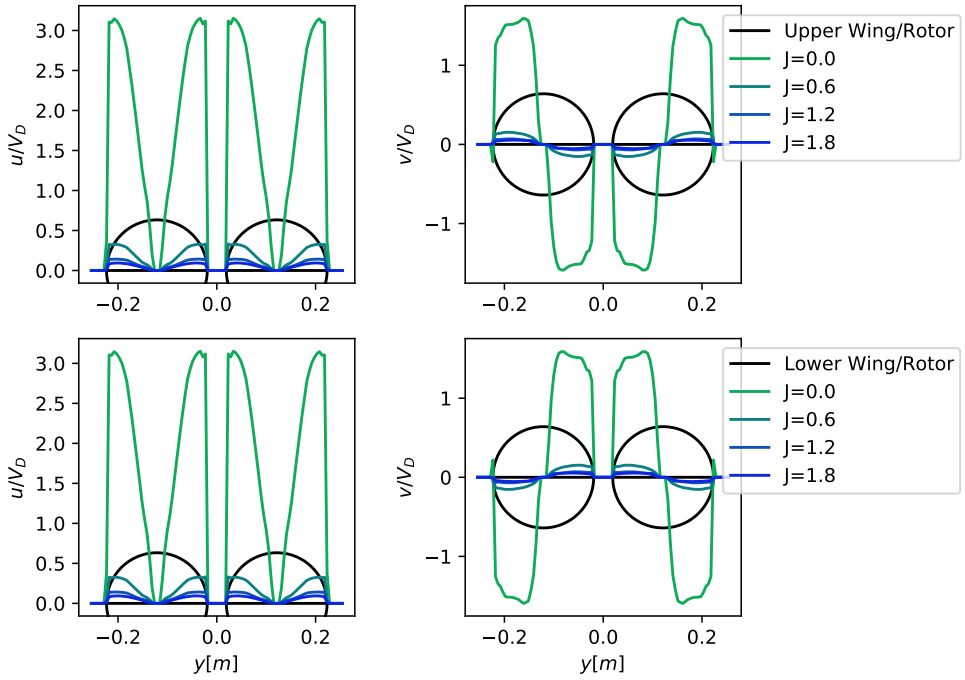

Fig. 4 Spanwise distributions of normalized axial and swirl components of the rotor wake velocity at various advance ratios. Solid black lines indicate the wing and rotor positions.

2. VLM Wing Model

We model wings using a VLM, discretizing the half-span with a 100×1 (spanwise by chordwise) lattice with cosine spacing. To determine the number of panels to use, we perform a convergence study on angle of attack, RPMs of upper and lower wings, and power requirements at the minimum-power trim condition for steady, level flight (see Fig. 5). Because the rotor wake has a significant effect on the lift distribution and therefore the solution of the VLM, and recognizing that the relative influence of the rotor wake changes throughout the transition trajectory, we test convergence at various trim velocities. Specifically, we test at the following scenarios:

- V_∞ is small compared to V_D
- stall constraint is active
- stall constraint is marginally active
- V_∞ is large compared to V_D

To account for wing-on-wing interactions, we satisfy the no-flow boundary condition at control points on both wings simultaneously. To capture interactions with the rotors, we interpolate the solved rotor wake velocity onto the vortex lattice. To preclude stall from the flight envelope, we constrain the sectional lift coefficient $c_l < c_{l,\text{stall}}$ in the trajectory optimization, assuming the stall lift coefficient $c_{l,\text{stall}} = 1.3$.

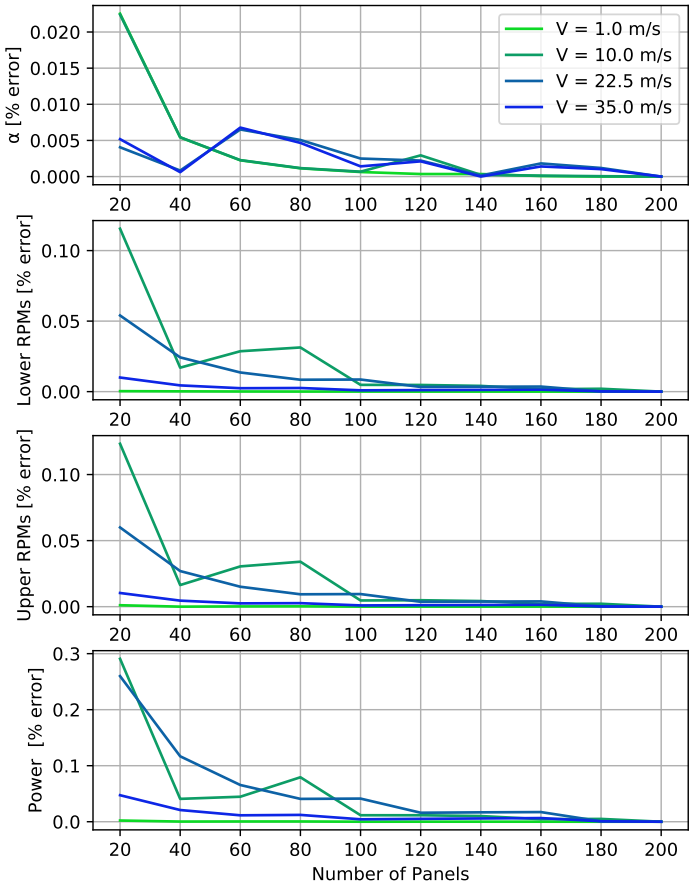

Fig. 5 The VLM converges most quickly when the rotor wake is comparatively insignificant (high velocities), or when wing aerodynamics are comparatively insigificant (low velocities). Note that error is referenced with respect to the 100 panel model.

3. Drag

In addition to the induced drag, which is accounted for by the VLM, we model the parasitic drag of the aircraft using a drag coefficient $C_{D_P} = 0.0151$, consistent with [16], and where we let V_∞ be the velocity at the rotor disk V_D.

C. Total Aerodynamic Forces and Moments

With $F(\mathbf{x}, \mathbf{u}) = \begin{bmatrix} F_x, & F_y \end{bmatrix}^\top$ being the x and y components of the aerodynamic force acting on the vehicle in the body frame, and $M(\mathbf{x}, \mathbf{u})$ being the net aerodynamic moment about the vehicle's center of mass, we have for the VLM+BEM model:

$$F(\mathbf{x}, \mathbf{u}) = F_{\text{VLM}} + 2T_{\text{upper}} + 2T_{\text{lower}} - D_P \tag{7}$$

$$M(\mathbf{x}, \mathbf{u}) = M_{\text{VLM}} + s(2T_{\text{upper}} - 2T_{\text{lower}}). \tag{8}$$

III. Dynamics

Our dynamic model takes the form $\dot{\mathbf{x}} = f(\mathbf{x}, \mathbf{u})$, where $\mathbf{x}$ and $\mathbf{u}$ are respectively the states and inputs of the nonlinear bi-wing tailsitter dynamics. We define $\mathbf{x}$ and $\mathbf{u}$ as

$$\mathbf{x} = \begin{bmatrix} p \\ v \\ \theta \\ \dot{\theta} \end{bmatrix}, \qquad \mathbf{u} = \begin{bmatrix} u_1 \\ u_2 \end{bmatrix} \tag{9}$$

where $p = \begin{bmatrix} p_x, & p_y \end{bmatrix}^\top$ are the forward and upward components of the position of the aircraft with respect to some fixed inertial frame, $v = \begin{bmatrix} v_x, & v_y \end{bmatrix}^\top$ are the forward and upward components of the velocity vector expressed in the body frame of the vehicle with respect to the inertial frame, θ is the rotation angle from the x-axis of the inertial frame to the x-axis of the body frame, and $\dot{\theta}$ is its time derivative. The body frame of the vehicle refers to the coordinate system whose origin lies at the vehicle center of mass and whose x- and y-axes point out the nose and wings of the vehicle respectively. When using the actuator disk rotor model, $\mathbf{u} = [V_{\text{upper}}, V_{\text{lower}}]^\top$ is the velocity induced by the upper and lower rotors, and when using the BEM rotor model, $\mathbf{u}$ is the RPMs of the upper and lower rotors. See Fig. 1 for a depiction of these values. Also depicted is the relationship $\theta = \gamma + \alpha$, where γ is the flight path angle, and α is the angle of attack.

The full dynamic model of the aircraft is given by

$$\dot{\mathbf{x}} = f(\mathbf{x}, \mathbf{u}) = \begin{bmatrix} \dot{p} \\ \dot{v} \\ \dot{\theta} \\ \ddot{\theta} \end{bmatrix} = \begin{bmatrix} Rv \\ -gR^\top e_2 + \frac{1}{m} F(\mathbf{x}, \mathbf{u}) - \dot{\theta} \begin{bmatrix} 0 & -1 \\ 1 & 0 \end{bmatrix} v \\ \dot{\theta} \\ \frac{1}{I} M(\mathbf{x}, \mathbf{u}) \end{bmatrix}, \qquad R = \begin{bmatrix} \cos\theta & -\sin\theta \\ \sin\theta & \cos\theta \end{bmatrix} \tag{10}$$

where g is the gravitational acceleration constant, m is the mass of the vehicle, I is its rotational inertia, and $e_2 = [0, \ 1]^\top$. For this vehicle, we assume the moment of inertia about the pitch axis to be $I = 0.011$ kg m^2.

A summary of model coefficients and their chosen values is given in Tab. 1.

IV. Optimal Trajectory Generation and Control

We formulate the takeoff and transition problem in two steps. First, we find feasible, minimum power initial and final states and control inputs as described in Sec. IV.A. Then, we use these as endpoint constraints in an optimal control problem to find the minimum time or energy trajectory to transition between these states as described in Sec. IV.B. Both nonlinear optimization problems are solved using the SNOPT gradient-based optimizer [26].

A. Finding feasible initial and final states

We first find feasible initial and final states ($\mathbf{x}_0$ and $\mathbf{x}_f$) and control inputs ($\mathbf{u}_0$ and $\mathbf{u}_f$) which satisfy trimmed flight for some desired airspeed V_d at an angle γ above the horizon.

Trimmed flight is a state in which the vehicle travels with a constant airspeed, angle of attack, and throttle, and at which translational and rotational accelerations are zero. More formally, trim flight occurs when

$$\dot{\mathbf{x}} = \dot{\mathbf{x}}_d \triangleq \begin{bmatrix} V_d \cos\gamma & V_d \sin\gamma & 0 & 0 & 0 & 0 \end{bmatrix}^\top. \tag{11}$$

Table 1 Constants and parameters used in modeling the CRC-3 bi-wing VTOL.

Symbol	Value	Description
m	1.36 kg	Vehicle mass
I	0.0111 kg m^2	Inertia about the pitch axis
g	9.81 m s^{-2}	Acceleration due to gravity
ρ	1.225 kg^3 m^{-1}	Air density
s	0.25 m	Spacing between wings
b	0.508 m	Wingspan
AR	5.904	Wing aspect ratio
λ	1.0	Taper ratio
Λ	0.0	Sweep angle
ϕ	0.0	Dihedral
θ_r	0.0	Root twist
θ_t	0.0	Tip twist
N_p	100	Number of panels
d_r	0.2041 m	Rotor diameter
C_{D_P}	0.0151	Parasitic Drag Coefficient

For a traditional aircraft with a single row of rotors, there exists one unique trimmed state for a given velocity. However, the second row of rotors on the biplane provides arbitrary moment control for fixed thrust, meaning multiple trimmed states may exist for a given velocity. We desire to find the trim state that minimizes the input power $P(\mathbf{x}, \mathbf{u})$. Trim calculation can then be written as an optimization problem of the form

$$\begin{aligned} &\text{minimize} && P(\mathbf{x}, \mathbf{u}) \\ &\text{w.r.t.} && \mathbf{u},\ \alpha,\ \gamma \\ &\text{subject to} && \dot{\mathbf{x}} - \dot{\mathbf{x}}_d = \mathbf{0} \\ & && \dot{\mathbf{x}} = f(\mathbf{x}, \mathbf{u}) \\ & && 0 < \gamma < \frac{\pi}{2} \\ & && \theta = \gamma + \alpha \\ & && c_l < c_{l,\text{stall}}. \end{aligned} \tag{12}$$

For the low fidelity model, the stall constraint is written in terms of the wing lift coefficient $C_L < C_{L,\text{stall}}$. The stall constraint makes it impossible to find a trimmed condition for steady level flight ($\gamma = 0$) at velocities below stall speed. However, for some $0 < \gamma < \pi/2$, we can trim the aircraft at a much wider range of velocities. As shown in Fig. 6, the low fidelity method and the mid fidelity method neglecting swirl trim successfully at all $V_d > 0$, while the mid fidelity method including swirl trims only for $V_d \gtrsim 10$ m/s.

We further note that a climbing attitude increases the power requirement, implying that γ is encouraged to decrease to its minimum value. Therefore, we conclude that the γ in Fig. 6 represents the smallest possible $0 < \gamma < \pi/2$ allowed for a feasible trim state. The fact that $\gamma > 0$ indicates climb may explain the enormous difference in power requirement between the models, which becomes as high as 90% at a trim velocity of roughly 12.5 m/s. We note that in this case, $\gamma > 0$ for the mid fidelity (higher power) model, indicating it is climbing, while $\gamma = 0$ for the low fidelity model, indicating steady level flight. Where $\gamma = 0$ for all models, the power is indistinguishable between mid fidelity models, and is greater for the mid fidelity models than for the low fidelity model. This discrepancy starts on the order of 10% and increases with velocity until it is roughly 50% at $V_d = 30$ m/s.

By comparing with Fig. 7 we can see that the point at which γ reaches 0 is the point at which the stall constraint is no longer active in the trim optimization. This is also the steady level flight stall speed for the aircraft.

We note that the stall constraint lifts at the lowest V_d for the low fidelity model, next for the mid fidelity model neglecting swirl, and finally for the mid fidelity model including swirl, implying that the mid fidelity models are more

stall constrained than the low fidelity model. This follows intuition: the low fidelity model applies an average wake velocity across the wing uniformly, while the mid fidelity models account for a distributed wake velocity. This results in higher maximum local lift coefficients than would occur were the wake velocity uniform. Further, under this hypothesis, we point out a difference in stall speeds of nearly 3 m/s between low and mid fidelity models.

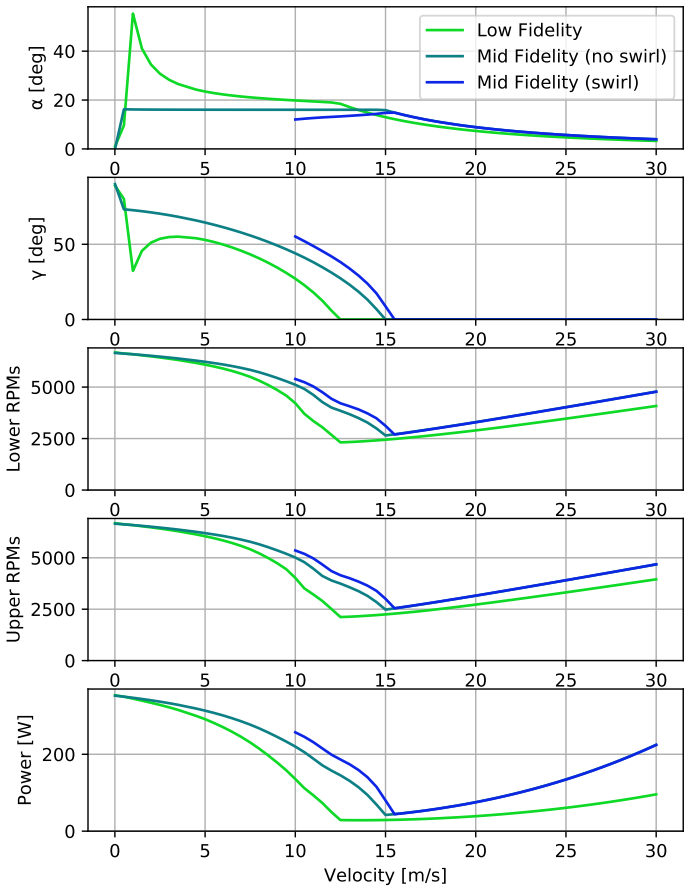

Fig. 6 Trim comparison of our three aerodynamic models at increasing velocities.

B. Trajectory Optimization

Our aim is to find optimal takeoff trajectories that take the aircraft, represented by the dynamic system in Eq. 10, from an initial state $\mathbf{x}_0$ to a final state $\mathbf{x}_f$ while remaining above the ground ($p_y \geq 0$), at a valid pitch angle ($-\frac{\pi}{2} \leq \theta \leq \frac{\pi}{2}$), and avoiding stall ($c_l < c_{l,\text{stall}}$). The objective we consider is minimizing the energy consumption over the duration of the trajectory,

$$J_{\text{energy}} = \int_{t_0}^{t_f} P(\mathbf{x}, \mathbf{u}) dt. \tag{13}$$

To perform the trajectory optimization, we use direct collocation with trapezoidal quadrature as described in [27]. In this method, we represent the state $\mathbf{x}$ of the dynamical system using quadratic (second order) splines, and we represent the control input $\mathbf{u}$ as linear (first order) splines. These splines are approximated at a series of N_t collocation points which are uniformly spaced in time. This allows us to approximate the minimum control objective function as

$$J_{\text{energy}} = \int_{t_0}^{t_f} P(\mathbf{x}, \mathbf{u}) dt \approx \sum_{k=0}^{N_t-1} \frac{1}{2}(P(\mathbf{x}_k, \mathbf{u}_k) + P(\mathbf{x}_{k+1}, \mathbf{u}_{k+1}))h_k, \tag{14}$$

where t_0 is the initial time, t_f is the final time, and $h_k = t_{k+1} - t_k = t_f / N_t$. We can use the trapezoid rule to

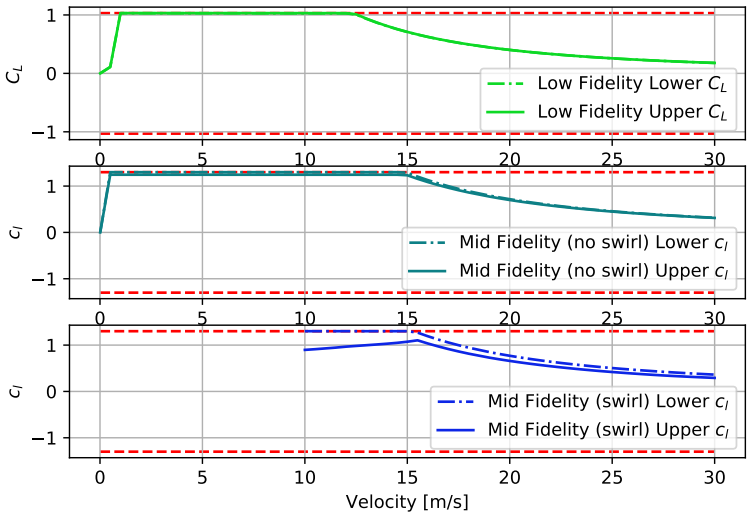

Fig. 7 Comparison of lift coefficients at trim for our three aerodynamic models.

approximately integrate the system dynamics $f(\mathbf{x}, \mathbf{u})$ by evaluating them at each collocation point

$$\mathbf{x}_{k+1} - \mathbf{x}_k = \int_{t_k}^{t_{k+1}} \dot{\mathbf{x}} ds \tag{15}$$

$$= \int_{t_k}^{t_{k+1}} f(\mathbf{x}, \mathbf{u}) ds \tag{16}$$

$$\approx \frac{1}{2} h_k (f(\mathbf{x}_{k+1}, \mathbf{u}_{k+1}) + f(\mathbf{x}_k, \mathbf{u}_k)) \tag{17}$$

where $\mathbf{x}_k = \mathbf{x}(t_k)$, $\mathbf{u}_k = \mathbf{u}(t_k)$. We then enforce these dynamics as equality constraints,

$$\mathbf{x}_{k+1} - \mathbf{x}_k = \frac{1}{2} h_k (f(\mathbf{x}_{k+1}, \mathbf{u}_{k+1}) + f(\mathbf{x}_k, \mathbf{u}_k)). \tag{18}$$

This results in the optimization

$$\begin{aligned}
&\text{minimize} && J_{\text{energy}}(\mathbf{u}, t_f) \\
&\text{w.r.t.} && t_f, \mathbf{x}_k, \mathbf{u}_k \text{ for } k \in [0, \ldots, N] \\
&\text{subject to} && \mathbf{x}(t_0) = \mathbf{x}_0, \quad \mathbf{x}(t_f) = \mathbf{x}_f, \\
& && \mathbf{u}(t_0) = \mathbf{u}_0^*, \quad \mathbf{u}(t_f) = \mathbf{u}_f^*, \\
& && p_y \geq 0, \quad -\frac{\pi}{2} \leq \theta \leq \frac{\pi}{2}, \quad t_f > t_0 \\
& && C_{L_k} < C_{L,\text{stall}} \\
& && \mathbf{x}_{k+1} - \mathbf{x}_k = \frac{1}{2} h_k (f(\mathbf{x}_{k+1}, \mathbf{u}_{k+1}) + f(\mathbf{x}_k, \mathbf{u}_k)),
\end{aligned} \tag{19}$$

V. Results and Discussion

The following subsections show results from verifying our trajectory optimization framework, computation of the initial and final states, and computation and comparison of takeoff and transition trajectories.

A. Initial and Final States

We use Eq. 12 with the low fidelity model to compute the γ, α, and $\mathbf{u}$ that will achieve the desired initial and final velocities given above. The results from these computations are in Table 2 and Table 3.

Table 2 Initial pitch and control inputs for $V_{d_0} = 1$ m/s.

γ_0	90.0°
α_f	0°
$\mathbf{u}_0$	$[6540.6,\ 6540.6]^\top$ RPM

Table 3 Final pitch and control inputs for $V_{d_f} = 20$ m/s.

γ_f	0°
α_f	4.7181°
$\mathbf{u}_f$	$[3461.2,\ 3461.2]^\top$ RPM

B. Verification

To verify our optimization framework, we set up a path whose start and end points are at the same altitude and velocity, and find the trajectory that minimizes energy consumption. The well-known solution is a constant, trimmed, minimum power state. After comparing, discrepancies appear to be within machine error.

C. Comparison of Trajectories

In our simulations we found the computational complexity of the mid fidelity models to be too high for our existing optimization framework (though, as we will soon discuss, we believe it to be quite possible). For this reason, we find trajectories using the low fidelity model and integrate the obtained control sequence on the mid fidelity models to assess the shortcomings of the low fidelity model. This is akin to analyzing the behavior of the optimal low-fidelity trajectories as feed-forward trajectories on an experimental aircraft.

In Figs. 8-10 we compare the minimum energy trajectory for takeoff transition using the three aerodynamic models. First, we note that the power quickly reaches its maximum within the first half second as the aircraft climbs, peaking shortly and dropping suddenly. As power drops, C_L rises, hits its stall constraint, and plateaus over 0.5 s $\lesssim t \lesssim$ 1.5 s. Then the lift coefficient begins to drop, maintaining a near linear decrease until it reaches its final state. This suggests it may be energetically favorable to expend a large amount of energy to gain momentum and then coast, conserving energy overall.

From Fig. 8, we observe that the mid fidelity model including swirl responds poorly to the control values computed on the low fidelity model. One possible reason becomes clear as we examine the role of stall in each method. From Fig. 10 we can see that while the low fidelity model successfully avoids stall throughout the transition maneuver, the mid fidelity models do not. The maximum local lift coefficient of the mid fidelity models including and neglecting swirl were roughly bounded by $[-60, 60]$ and $[-60, 20]$ (not in the figure), respectively, in regions where stall would certainly be encountered. The mid fidelity neglecting swirl spends roughly a third of its time violating the stall constraint, while the mid fidelity model including swirl spends roughly half its time violating stall. We conclude that the optimal trajectory according to the low fidelity model is infeasible for the mid fidelity models due to the stall constraint. Assuming the mid fidelity models indeed capture the relevant physics more accurately, the optimized trajectory would lead to problems if attempted in hardware, and would rely heavily on a controller to correct. The low fidelity model predicts stall too loosely, and requires a correction factor of some kind if it is to be used.

We also note the extreme difference between the mid fidelity trajectories in Fig. 8. We then conclude that including the swirl velocity in the aerodynamic model has a significant effect on the trajectory, as the inclusion of swirl is the unique difference between the two mid fidelity methods.

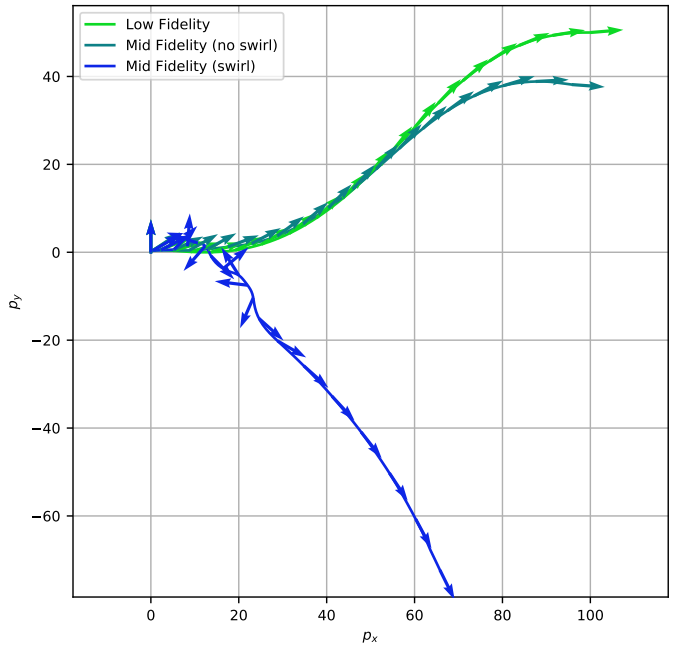

Fig. 8 Optimal takeoff trajectory computed with low fidelity model and integrated using mid fidelity models with and without swirl enabled. Arrows indicate the pitch of the vehicle.

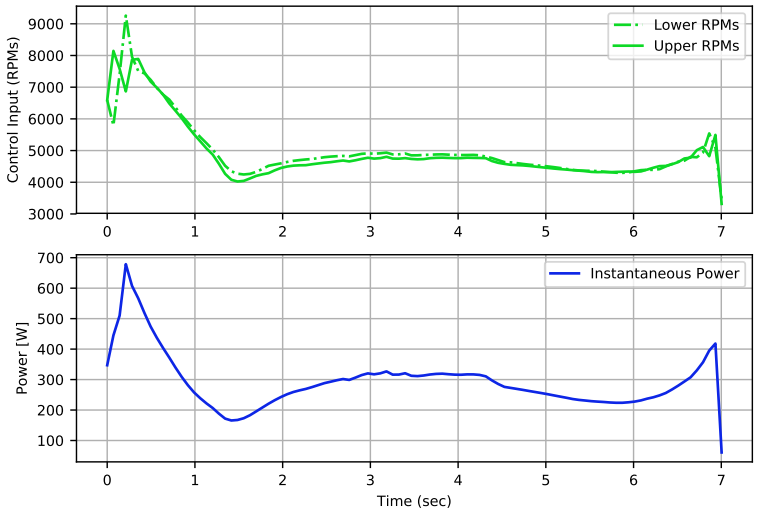

Fig. 9 Optimized control inputs and instantaneous power along the optimal trajectory shown in Fig. 8.

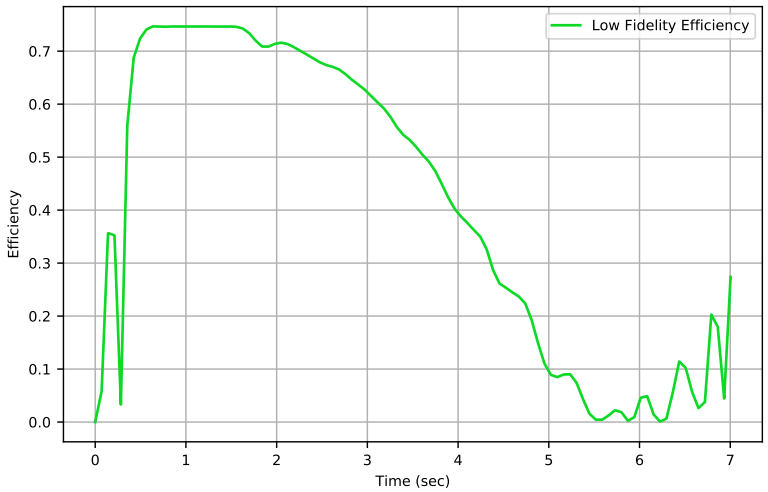

Fig. 11 Oswald efficiency number for the low fidelity optimal trajectory.

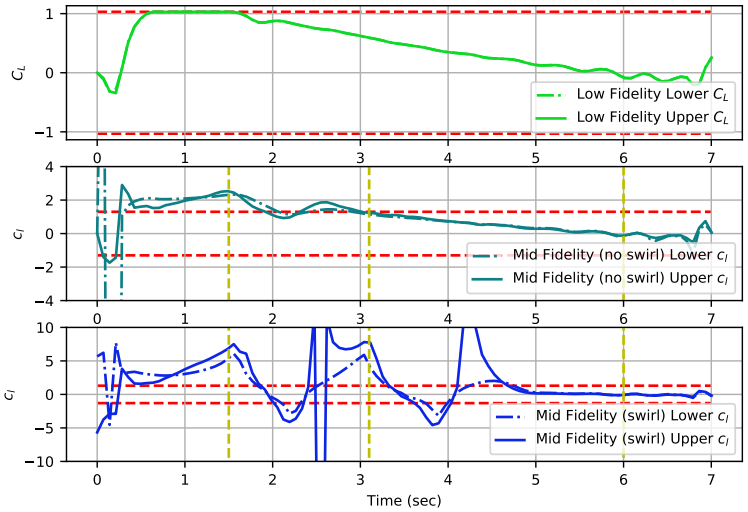

Fig. 10 Lift coefficients nearest stall vs. time for the optimal takeoff transition. Note that both mid fidelity methods violate their stall constraints (in red) for the majority of the trajectory. Dashed gold lines at t = 1.5, 3.1, and 6.0 seconds mark when lift distributions are plotted in Fig. 12.

From Fig. 6, we conclude that a stall-free transition trajectory exists for these methods, and can be obtained by smoothly transitioning through trimmed velocities from zero ground speed to the desired cruise velocity, as shown by [6]. It should be noted that while trim does not appear to be feasible for all airspeeds–e.g., no trim states exist for the mid fidelity model including swirl between $0 < V_d \lesssim 10$ m/s–we can require an initial velocity of 10 m/s with $\gamma = 90°$ to begin the maneuver, essentially accelerating directly upwards. The wing experiences no net lift, and the aircraft may successfully climb to the desired velocity. Once it reaches its minimum trim velocity, it can begin to transition through trimmed states until it reaches a cruise state. In a future work, we may implement these optimizations to more fully compare the models. For now, we simply show that trajectories obtained using the simplest interference model are infeasible according to a higher fidelity model, suggesting the importance of using such a model in path planning. This does not necessarily make these models superior. Their computational cost would highly restrict their use in just-in-time trajectory planning. It is possible that the low fidelity model could perform adequately with a correction factor.

There are inherent differences between the three aerodynamic models that are illustrated by their trimmed states in Fig. 6. Note that both mid fidelity models predict higher power requirements (up to a 40 times increase) than the low

fidelity model at lower V_d, but lower power requirements (on the order of 10% at V_d = 40 m/s) after the stall constraint is no longer active.

We observe this difference in lift distribution between models in Fig. 12. Here, we plot the spanwise lift distribution of upper and lower wings at the states where stall is most violated for the swirl model (t = 1.5 seconds), where the stall constraint just lifts (t = 3.1 seconds), and where the stall constraint is far from active (t = 6.0 seconds). We note the outboard increase in lift distribution in the swirl model for the upper wing, as well as the inboard increase in lift distribution for the lower wing, which matches the rotor orientation (outboard up for the upper wing and inboard up for the lower wing). To preserve fair comparison, we remark that distributions for the swirl and no swirl models are calculated at very different states (see Fig. 10), and should be considered separately.

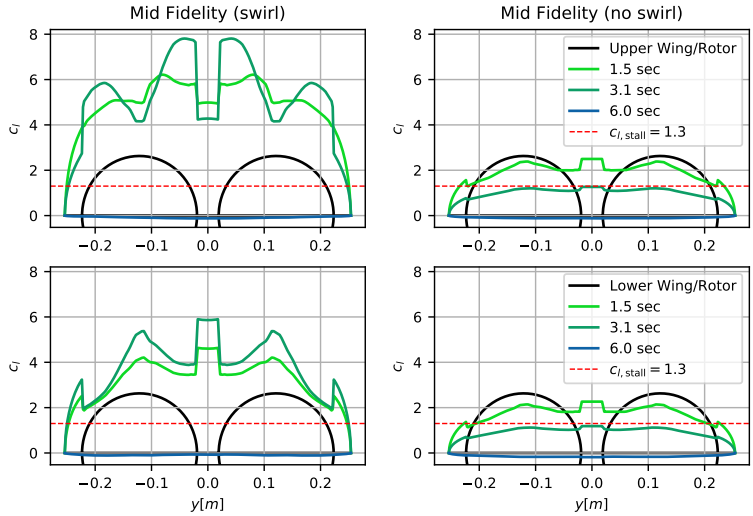

Fig. 12 Lift distributions for the mid fidelity models at locations marked by the dashed gold lines in Fig. 10. Note how inclusion of the swirl velocity affects the lift distribution, making stall more likely. Circles denote rotor discs in x-axis units.

VI. Conclusion

In the present work, we compare the performance of three aerodynamics methods for generating minimum energy takeoff transition trajectories. Each captures a different level of aerodynamic interaction between rotors and wings. The low fidelity model captures a rudimentary influence of rotor wake on the wing using momentum theory and applying the average rotor wake uniformly over the wing. The mid fidelity models apply the rotor wake velocity distribution as obtained using the BEM, neglecting and including the swirl component of velocity, respectively. The models were calibrated to have the same lift polars in the absence of rotors, and to have the same rotor thrust and power coefficients. Each model differs primarily by its interaction model.

We compare trim states obtained using each of the models, and find that the low fidelity model predicts a stall speed roughly 3 m/s lower than the mid fidelity models. The low fidelity model also predicts a difference in power requirement on the order of 10% lower at the mid fidelity models' stall speed. This discrepancy increases with velocity to roughly 50% for steady level flight. Power is predicted more conservatively by the mid fidelity models in all cases.

We optimize the minimum-energy transition trajectory using gradient-based optimization and direct collocation with the low fidelity model. We then simulate the trajectory using the mid fidelity models by using the same rotor RPMs obtained from the optimization. The difference in stall constraints between the models makes the optimized trajectory infeasible for the mid fidelity models without violating stall. The mid fidelity models differ significantly in their performance—the mid fidelity model neglecting swirl behaves qualitatively similarly to the low fidelity model, while the mid fidelity model including swirl behaves altogether differently.

Therefore, we conclude that modeling the swirl component of velocity plays a significant role that should be considered in trajectory optimization. We also conclude that the stall constraint and swirl velocity play a significant role in the transition maneuver and warrant careful consideration. We recommend future efforts to perform trajectory optimization using the higher fidelity models, as well as to validate models of wing-rotor interactions that capture swirl

and stall constraints in hardware. We further recommend efforts to develop reduced order methods that capture these phenomena, for example, incorporating the Tangler and Ostowari[9] stall model. Obtaining and validating such a model is invaluable to finding the optimal takeoff trajectory for a bi-wing tailsitter.

References

[1] Heydari, M., and Sadat, H., "A reduced order model for prediction of aerodynamic loads on an unmanned aerial system with hybrid quadcopter biplane configuration," *APS*, 2019, pp. G41–005.

[2] Avera, M., and Singh, R., "Scalability of Hybrid-Electric Propulsion for VTOL UAS," n.d.

[3] Theodorsen, T., "Optimum Path of an Airplane–Minimum Time to Climb," *Journal of the Aerospace Sciences*, Vol. 26, No. 10, 1959, pp. 637–642.

[4] Betts, J. T., *Practical Methods for Optimal Control and Estimation Using Nonlinear Programming*, Vol. 19, Siam, 2010.

[5] Van Nieuwstadt, M. J., and Murray, R. M., "Real-Time Trajectory Generation for Differentially Flat Systems," *International Journal of Robust and Nonlinear Control: IFAC-Affiliated Journal*, Vol. 8, No. 11, 1998, pp. 995–1020.

[6] Droandi, G., Syal, M., and Bower, G., "Tiltwing Multi-Rotor Aerodynamic Modeling in Hover, Transition and Cruise Flight Conditions," *AHS International 74th Annual Forum & Technology Display*, 2018.

[7] Oosedo, A., Abiko, S., Konno, A., and Uchiyama, M., "Optimal Transition from Hovering to Level-Flight of a Quadrotor Tail-Sitter UAV," *Autonomous Robots*, Vol. 41, No. 5, 2017, pp. 1143–1159.

[8] Chauhan, S. S., and Martins, J. R. R. A., "Tilt-Wing eVTOL Takeoff Trajectory Optimization," *Journal of Aircraft*, Vol. 57, No. 1, 2020, pp. 93–112. https://doi.org/10.2514/1.C035476, URL https://doi.org/10.2514/1.C035476.

[9] Tangler, J. L., and Ostowari, C., "Horizontal axis wind turbine post stall airfoil characteristics synthesization," 1995.

[10] Hrishikeshavan, V., Bogdanowicz, C., and Chopra, I., "Design, Performance and Testing of a Quad Rotor Biplane Micro Air Vehicle for Multi Role Missions," *International Journal of Micro Air Vehicles*, Vol. 6, No. 3, 2014, pp. 155–173.

[11] Veldhuis, L. L. M., "Review of Propeller-Wing Aerodynamic Interference," *24th International Congress of the Aeronautical Sciences*, 2004. URL http://icas.org/ICAS{_}ARCHIVE/ICAS2004/PAPERS/065.PDF.

[12] Montagnani, D., Tugnoli, M., Fonte, F., Zanotti, A., Syal, M., and Droandi, G., "Mid-Fidelity Analysis of Unsteady Interactional Aerodynamics of Complex VTOL Configurations," *45th European Rotorcraft Forum (ERF 2019)*, 2019, pp. 1–11.

[13] Witkowski, D. P., Lee, A. K., and Sullivan, J. P., "Aerodynamic interaction between propellers and wings," *Journal of Aircraft*, Vol. 26, No. 9, 1989, pp. 829–836. https://doi.org/10.2514/3.45848.

[14] Alvarez, E., Ning, A., Multirotor, M., and Alvarez, E. J., "Modeling Multirotor Aerodynamic Interactions Through the Vortex Particle Method," *AIAA Aviation Forum*, 2019, p. 3191. https://doi.org/10.2514/6.2019-2827, URL https://scholarsarchive.byu.edu/facpubhttps://scholarsarchive.byu.edu/facpub/3191.

[15] Thom, A., and Duraisamy, K., "Computational Investigation of Unsteadiness in Propeller Wake–Wing Interactions," *Journal of Aircraft*, Vol. 50, No. 3, 2013, pp. 985–988.

[16] Reddinger, J.-P., McIntosh, K., Zhao, D., and Mishra, S., "Modeling and Trajectory Control of a Transitioning Quadrotor Biplane Tailsitter," 2019.

[17] McIntosh, K., and Mishra, S., "Optimal Trajectory Generation for a Quadrotor Biplane Tailsitter," 2020.

[18] Bogdanowicz, C., Hrishikeshavan, V., and Chopra, I., "Development of a quad-rotor biplane MAV with enhanced roll control authority in fixed wing mode," *American Helicopter Society, 71st Annual Forum*, 2015.

[19] Alvarez, E. J., and Ning, A., "Development of a Vortex Particle Code for the Modeling of Wake Interaction in Distributed Propulsion," 2018, pp. 1–22. https://doi.org/10.2514/6.2018-3646.

[20] Selig, M., "Modeling full-envelope aerodynamics of small UAVs in realtime," *AIAA Atmospheric Flight Mechanics Conference*, 2010, p. 7635.

[21] Ning, A., "A Simple Solution Method for the Blade Element Momentum Equations with Guaranteed Convergence," *Wind Energy*, Vol. 17, No. 9, 2014, pp. 1327–1345. https://doi.org/10.1002/we.1636, URL http://dx.doi.org/10.1002/we.1636.

[22] Du, Z., and Selig, M., "A 3-D stall-delay model for horizontal axis wind turbine performance prediction," *1998 ASME Wind Energy Symposium*, 1998, p. 21.

[23] Eggers, A., Chaney, K., and Digumarthi, R., "An assessment of approximate modeling of aerodynamic loads on the UAE rotor," *ASME 2003 Wind Energy Symposium*, American Society of Mechanical Engineers Digital Collection, 2003, pp. 283–292.

[24] Viterna, L. A., and Janetzke, D. C., "Theoretical and experimental power from large horizontal-axis wind turbines," Tech. rep., National Aeronautics and Space Administration, Cleveland, OH (USA). Lewis . . . , 1982.

[25] Jung, Y. S., Govindarajan, B., and Baeder, J., "A Hamiltonian-strand approach for aerodynamic flows using overset and hybrid meshes," *72nd Annual Forum of the American Helicopter Society*, 2016.

[26] Gill, P. E., Murray, W., and Saunders, M. A., "SNOPT: An SQP Algorithm for Large-Scale Constrained Optimization," *SIAM Review*, Vol. 47, No. 1, 2005, pp. 99–131. https://doi.org/10.1137/S0036144504446096.

[27] Kelly, M., "An Introduction to Trajectory Optimization: How to do Your Own Direct Collocation," *SIAM Review*, Vol. 59, No. 4, 2017, pp. 849–904.